Sequence Impedance Modeling and Analysis of MMC in Single-Star Configuration

Yang Zhang, *Student Member, IEEE*, Xin Chen, *Member, IEEE*, and Jian Sun, *Fellow, IEEE*

***Abstract*—This paper presents sequence impedance modeling and analysis of modular multilevel converters (MMCs) in a single-star configuration for static VAR compensation (STATCOM) application. Prior work on impedance modeling of MMC is limited to the double-star configuration for high-voltage dc transmission applications. Compared to that, single-star configuration uses only a single arm of switching modules in each phase, eliminating the second-harmonic circulating current and the need for the associated circulating current control. On the other hand, the lack of connection to a stiff dc bus makes it essential to include module capacitor voltage control in the model. A special form of the multi-harmonic linearization method is applied to take advantage of the simpler harmonic spectra and to reduce the complexity of the resulting models. The developed models are verified by simulation and experiment, respectively, and used to understand the similarities and differences in the impedance characteristics of the two configurations as well as the effects on stability. A representative wind power plant is presented as an example to demonstrate the application of STATCOM impedance models on the system stability analysis.**

***Index Terms*—Harmonic linearization, impedance modeling, modular multilevel converters (MCCs), STATCOM.**

I. Introduction

SEQUENCE impedance modeling and analysis is an effective method to study stability and resonance of power electronics connected to the power grid. Small-signal sequence impedance models have been developed for various types of converters and converter systems, such as type-III and type-IV turbines [1]–[4] and high-voltage dc (HVDC) converters [5], [6], to support this application. Because these converters operate with sinusoidal voltage and/or current, linearization of their models, which is necessary for the development of sequence impedance

Manuscript received January 6, 2019; revised March 9, 2019; accepted April 10, 2019. Date of publication April 17, 2019; date of current version October 18, 2019. This work was supported in part by the Science and Technology Project "Impedance-Based Modeling and Control of Distributed Generation Systems" (NYB1720170218), funded by the State Grid Corporation of China, in part by the National Natural Science Foundation of China under Grant 51877105, and in part by Jiangsu Postgraduate Research and Practical Innovation Project KYLX16_0360. Recommended for publication by Associate Editor Herbert H.-C. Iu. *(Corresponding author: Xin Chen.)*

Y. Zhang and X. Chen are with the Jiangsu Key Laboratory of New Energy Generation and Power Conversion, Nanjing University of Aeronautics and Astronautics, Nanjing 210016, China (e-mail:

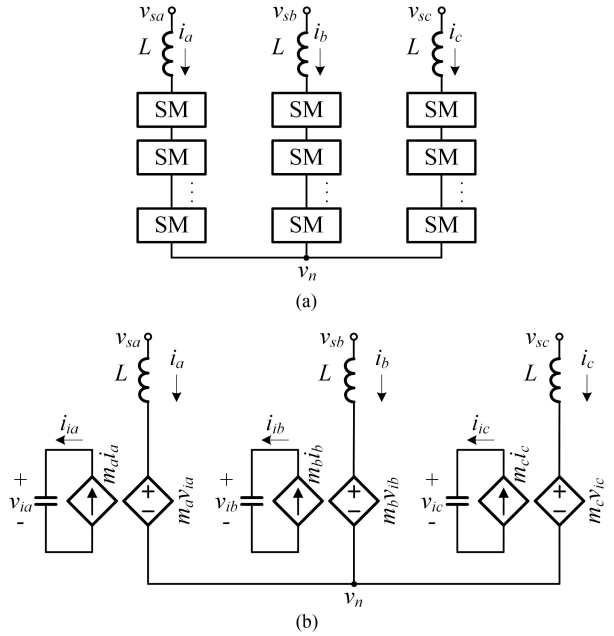

Fig. 1. Power stage of an MMC in single-star configuration. (a) Main circuit. (b) Continuous approximate model.

such harmonics in the small-signal model, which provides an opportunity to develop a lower-order model.

The purpose of this paper is to present small-signal sequence impedance modeling and analysis of MMC in the single-star configuration. Compared to the previous work on the modeling of MMC in double-star configuration, this work emphasizes the following.

1) A simplified form of the multi-harmonic linearization method by taking advantage of the absence of second-harmonic circulating current.
2) Inclusion of module capacitor voltage control in the small-signal model.
3) The effects of these features on impedance characteristics of the converter.
4) Experimental validation of the developed model by a scale-down prototype.

The rest of the paper is organized as follows. Section II describes the circuit and control of MMC in the single-star configuration. Section III develops the converter impedance model based on double-harmonic linearization and uses a block diagram of small signal flow to represent this model. Section IV verifies the developed impedance models by detailed circuit simulation and experimental measurement of a scale-down prototype. Section V discusses the impedance characteristics of the single-star MMC by comparison with the double-star configuration. Section VI presents an application of the stability analysis of a representative wind power plant with STATCOM using this developed STATCOM impedance models. Section VII concludes the work.

II. Circuit and Control

Fig. 1(a) shows a simplified diagram of a three-phase MMC circuit in the single-star configuration. A full-bridge topology is commonly used as the switching module. Compared to the

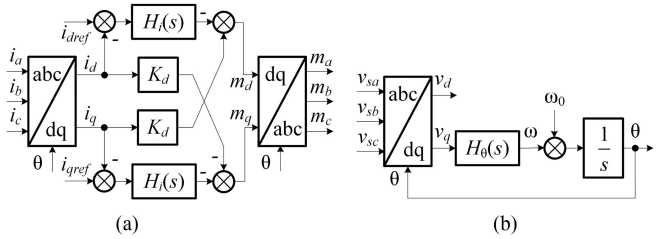

Fig. 2. Control functions of single-star MMC. (a) Phase current control. (b) PLL.

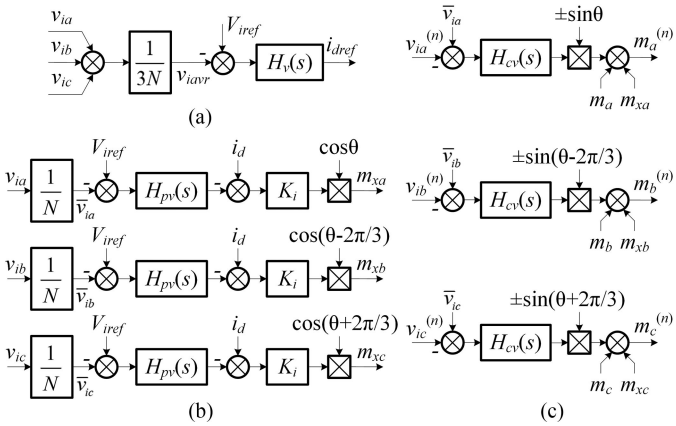

Fig. 3. Module capacitor voltage control of a STATCOM in single-star configuration. (a) Average voltage control. (b) Phase voltage balancing control. (c) Cell voltage balancing control for the *n*th sub-module.

double-star configuration, each phase here consists of only one arm. This difference in the converter circuit leads to several unique features in the operation and control of the single-star configuration that merits the work reported in this paper: harmonic-free arm current, no circulating current control, and no connection to a stiff dc bus. However, based on the symmetry between the upper and lower arms, the general form of a single-arm model of a double-star MMC modeled in [12] can also be applicable to the power stage of the single-star MMC.

The basic function for any MMC is phase current control, which is usually done by using a phase-locked loop (PLL) to synchronize with the PCC voltage and *dq*-frame current controller to regulate the currents, as depicted in Fig. 2. The *d*-axis and *q*-axis current reference represent the active and reactive current MMC, which are required to inject, respectively. The design and operation of these two control functions are similar to that of a double-star MMC, such that their corresponding small-signal control models modeled in [12] can be adopted as well. Circulating current control is important in the double-star configuration, but is not required here.

Since the absence of a connection to a stiff dc bus, the module capacitor voltage control becomes an integral part of single-star MMC control to maintain a stable and balanced module capacitor voltage. Functionally, this control is usually divided into three layers [19].

1) Average voltage control. Fig. 3(a) depicts an algorithm of average voltage control to regulate the average of all module capacitor voltages by using a PI compensator and adding a component to the *d*-axis reference of the phase current control.

2) Phase (Clustered) voltage balancing control. A number of algorithms can be used to achieve such function [20], where Fig. 3(b) presents a common method by reallocating the active power component in phase currents independently based on the average of module capacitor voltage in each phase. Noting that the phase voltage balancing is necessary for STATCOM operating with unbalanced grid voltages or to compensate for grid unbalance [21], [22]. Under such conditions, however, the symmetries identified in [12] among three phases are no longer true and additional harmonics may also appear. Therefore, a full-order power stage model with additional harmonics would be required, leading to a much more complex model. We will leave this for future work and focus in this paper on the balanced operation of STATCOM.
3) Cell (Individual) voltage balancing control. Fig. 3(c) depicts an algorithm of cell voltage control for carrier phase shifting pulsewidth modulation (PWM) to individually regulate each module capacitor voltage by using a PI compensator, and the operator before sinusoidal function depends on the operation mode of STATCOM [19]. However, since the average of module capacitor voltage in one phase is equal to any module capacitor voltages among this phase based on the assumption that the voltages are balanced at all time within each phase, this control actually doesn't affect dynamics of the converter, and we will ignore it in the small-signal model.

III. Impedance Modeling

A. Double-Harmonic Linearization

The starting point for the development of the desired frequency-domain small-signal model is the frequency-domain representation of key converter variables in Fig. 1(b). Without a second-harmonic circulating current in each phase, the arm current in the single-star configuration can be assumed harmonic-free in the steady-state operation, such that the control signal (insertion index) also contains no harmonics due to the feedback control of arm current presented in Fig. 2. On the other hand, the strong second-harmonic power flow caused by this sinusoidal arm current and insertion index leads to a second-harmonic component in the module capacitor voltage. When multiplied with the sinusoidal insertion index, this second-harmonic voltage has a trend to drive a third-harmonic current through the arm inductor. However, since this third harmonic is zero-sequence, it cannot actually flow.

Based on these, the arm current (**i**), insertion index (**m**), and equivalent module capacitor voltage ($\mathbf{v}_i$) can be represented in the frequency domain by a vector of complex Fourier coefficients as

$$\mathbf{i}=\begin{bmatrix}0\\ I_1e^{-j\alpha_1}\\ 0\\ I_1e^{j\alpha_1}\\ 0\end{bmatrix}\quad \mathbf{m}=\begin{bmatrix}0\\ M_1e^{-j\gamma_1}\\ 0\\ M_1e^{j\gamma_1}\\ 0\end{bmatrix}\quad \mathbf{v}_i=\begin{bmatrix}V_{i2}e^{-j\beta_2}\\ 0\\ V_{i0}\\ 0\\ V_{i2}e^{j\beta_2}\end{bmatrix}. \quad (1)$$

The coefficients are arranged in each vector according to their frequencies, starting from $-nf_1$ and ending at nf_1, with the dc component at the center. The arm current and insertion index vectors only contain a positive-sequence component at $\pm f_1$. The module capacitor voltage contains a dc and a second-harmonic negative-sequence component, but no higher order harmonics, such that the vectors in (1) can be defined to include up to the second harmonic ($\pm 2f_1$).

The frequency-domain representation (1) of the converter state and control variables leads to a frequency-domain model of the power stage where multiplication between two variables is replaced by convolution of the corresponding vectors. To develop a small-signal linearized model, the next step is to introduce a small-signal perturbation at an arbitrary frequency f_p to the grid voltage. Since the response to negative-sequence perturbation of a converter at frequency f_p can be obtained as the complex conjugate of its positive-sequence responses at frequency $-f_p$ [12], the development below will focus on the responses under the positive-sequence perturbation. Considering the nonlinearity in the converter model, this voltage perturbation will interact with the steady-state harmonics and cause a number of small-signal harmonics at frequencies that can be expressed as $f_p \pm if_1$, $i = 1, 2, \ldots$. With up to the second steady-state harmonic considered in (1), the frequencies of small-signal harmonics can be arranged in a vector form as

$$[f_p-2f_1, f_p-f_1, f_p, f_p+f_1, f_p+2f_1].$$

Accordingly, the grid voltage perturbation can be expressed in the frequency domain as

$$\hat{\mathbf{v}}_p=\begin{bmatrix}0\ 0\ \hat{V}_pe^{j\varphi_p}\ 0\ 0\end{bmatrix}^T$$

where $\hat{V}_p$ is the amplitude of the perturbation at f_p and φ_p is its initial phase angle. Similarly, small-signal responses of each of the variables defined in (1) can also be represented by a vector

$$\hat{\mathbf{i}}=\begin{bmatrix}\hat{I}_{p-2}e^{j\alpha_{p-2}}\\ \hat{I}_{p-1}e^{j\alpha_{p-1}}\\ \hat{I}_pe^{j\alpha_p}\\ \hat{I}_{p+1}e^{j\alpha_{p+1}}\\ \hat{I}_{p+2}e^{j\alpha_{p+2}}\end{bmatrix}\quad \hat{\mathbf{m}}=\begin{bmatrix}\hat{M}_{p-2}e^{j\gamma_{p-2}}\\ \hat{M}_{p-1}e^{j\gamma_{p-1}}\\ \hat{M}_pe^{j\gamma_p}\\ \hat{M}_{p+1}e^{j\gamma_{p+1}}\\ \hat{M}_{p+2}e^{j\gamma_{p+2}}\end{bmatrix}\quad \hat{\mathbf{v}}_i=\begin{bmatrix}\hat{V}_{ip-2}e^{j\beta_{p-2}}\\ \hat{V}_{ip-1}e^{j\beta_{p-1}}\\ \hat{V}_{ip}e^{j\beta_p}\\ \hat{V}_{ip+1}e^{j\beta_{p+1}}\\ \hat{V}_{ip+2}e^{j\beta_{p+2}}\end{bmatrix}. \quad (2)$$

Using these definitions, we can model the small-signal response of the converter by the following frequency-domain model [12]:

$$\hat{\mathbf{i}}=\mathbf{Y}_l[\hat{\mathbf{v}}_p-(\mathbf{M}\hat{\mathbf{v}}_i+\mathbf{V}_i\hat{\mathbf{m}})] \quad (3)$$

$$\hat{\mathbf{v}}_i=\mathbf{Z}_c\hat{\mathbf{i}}_i=\mathbf{Z}_c(\mathbf{M}\hat{\mathbf{i}}+\mathbf{I}\hat{\mathbf{m}}) \quad (4)$$

where steady-state matrices **I**, **M,** and $\mathbf{V}_i$ are formed based on the steady-state vectors defined in (1) [12], $\mathbf{Z}_c$ represents the impedance of equivalent module capacitor at small-signal

frequencies, defined as

$$\mathbf{Z}_c = \frac{1}{j2\pi C} \cdot \text{diag} \left[\frac{1}{f_p - 2f_1}, \frac{1}{f_p - f_1}, \frac{1}{f_p}, \frac{1}{f_p + f_1}, \frac{1}{f_p + 2f_1} \right]$$

and $\mathbf{Y}_l$ represents the admittance of arm inductor at small-signal harmonic frequencies, defined as

$$\mathbf{Y}_l = \frac{1}{j2\pi L} \cdot \text{diag} \left[\frac{1}{f_p - 2f_1}, 0, \frac{1}{f_p}, \frac{1}{f_p + f_1}, 0 \right].$$

Noting that the zero diagonal elements in $\mathbf{Y}_l$ correspond to frequencies of small-signal harmonics that form a zero-sequence among the three phases, and these elements are set to zero to eliminate zero-sequence current which cannot flow in the converter [12].

It should be pointed out that since the effects of second-harmonic circulating current in double-star MMC, the infinite number of harmonics, in theory, should be considered in multi-harmonic linearization. However, the amplitude of harmonic becomes progressively smaller as the frequency increases, such that only a small number of harmonics (up to the *n*th harmonic) would need to be considered in practice. Obviously, the correctness and accuracy of the small-signal model developed by multi-harmonic linearization depends on that selected harmonic truncation order. But the harmonic spectra becomes totally different in single-star MMC, without any harmonic truncation operations, the second harmonic is the only harmonic that should be considered in the small-signal modeling of single-star MMC. Based on this, the multi-harmonic linearization is naturally modified as double-harmonic linearization presented in this paper to greatly simplify the modeling process and reduce the order of matrix models without losses of the accuracy of developed models of single-star MMC.

B. Control Modeling

Basic MMC control functions such as phase current control and synchronization to the grid voltage by a PLL have been modeled in [12], and is summarized in this paper. The phase current control model $\mathbf{Q}_i$ is

$$\mathbf{Q}_i = \text{diag}\left[H_i(j2\pi(f_p - f_1)) + jK_d, 0, H_i(j2\pi(f_p - f_1)) - jK_d, 0, 0\right]. \quad (5)$$

The PLL model $\mathbf{P}_p$ is a zero matrix except for the (1, 3)th element, denoted as

$$G_\theta(j2\pi(f_p - f_1)) \cdot \{[H_i(j2\pi(f_p - f_1)) + jK_d] I_1 e^{-j\alpha_1} - M_1 e^{-j\gamma_1}\} \quad (6)$$

and the (3, 3)th element, denoted as

$$-G_\theta(j2\pi(f_p - f_1)) \cdot \{[H_i(j2\pi(f_p - f_1)) - jK_d] I_1 e^{j\alpha_1} - M_1 e^{j\gamma_1}\} \quad (7)$$

where

$$G_\theta(j2\pi f_p) = T_\theta(j2\pi f_p)/(1 + V_1 T_\theta(j2\pi f_p))$$
$$T_\theta(j2\pi f_p) = H_\theta(j2\pi f_p)/(j2\pi f_p).$$

Since module capacitor voltage control is unique in single-star MMC, the rest of this section is devoted to its modeling for inclusion in the over small-signal model. Considering first the average voltage control as depicted in Fig. 3(a), it can be expressed in small-signal form as

$$\hat{\mathbf{v}}_{iavr} = (\hat{\mathbf{v}}_{ia} + \hat{\mathbf{v}}_{ib} + \hat{\mathbf{v}}_{ic})/3N \quad (8)$$

where *N* is the number of the module in each arm. Since the summation in (8) cancels all positive and negative sequence components of the voltages among three phases, we can define a 5 × 5 diagonal matrix $\mathbf{T}_0$ to pick up the zero-sequence small-signal harmonics of one phase as

$$\hat{\mathbf{v}}_{iavr} = \mathbf{T}_0 \hat{\mathbf{v}}_i \quad (9)$$

where $\mathbf{T}_0$ is defined as $\mathbf{T}_0 = \text{diag}[0, 1, 0, 0, 1]$.

The average voltage control generates a reference for the *d*-axis current reference. This, in turn, contributes to the response of the insertion index in the *d*-axis through the *d*-axis current compensator. Based on this, the overall gain from the average module capacitor voltage to the *d*-axis insertion index can be written as

$$\hat{\mathbf{m}}_d = \mathbf{G}_v \hat{\mathbf{v}}_{iavr} \quad (10)$$

where $\mathbf{G}_v$ is a 5 × 5 diagonal matrix defined as

$$\mathbf{G}_v = \text{diag}[\{H_v(j2\pi(f_p + nf_1)) H_i(j2\pi(f_p + nf_1))\}|_{n=-2,-1,0,1,2}].$$

To convert (10) into the sequence domain, we denote that the insertion indexes in the phase and *dq*-frame are related to each other by

$$\begin{bmatrix} m_a \\ m_b \\ m_c \end{bmatrix} = \begin{bmatrix} \cos(2\pi f_1 t) & -\sin(2\pi f_1 t) \\ \cos(2\pi f_1 t - 2\pi/3) & -\sin(2\pi f_1 t - 2\pi/3) \\ \cos(2\pi f_1 t + 2\pi/3) & -\sin(2\pi f_1 t + 2\pi/3) \end{bmatrix} \begin{bmatrix} m_d \\ 0 \end{bmatrix}. \quad (11)$$

This is a nonlinear function and its small-signal response is obtained by convoluting $\hat{\mathbf{m}}_d$ defined in (10) with a vector representing each row of the matrix in (11). Considering the symmetry of three phases, we can express the relationship as

$$\hat{\mathbf{m}} = \mathbf{T}_c \hat{\mathbf{m}}_d \quad (12)$$

where $\mathbf{T}_c$ is a 5 × 5 tridiagonal matrix, of which elements in the main diagonal are zero, and elements in the diagonal above and below main diagonal are both 1/2.

By combining (9), (10), and (12), the model for this average voltage control is obtained and can be written as

$$\hat{\mathbf{m}} = \mathbf{T}_c \mathbf{G}_v \mathbf{T}_0 \hat{\mathbf{v}}_i. \quad (13)$$

The phase voltage balancing control is performed directly in the phase domain and on each phase independently, as depicted in Fig. 3(b). Since this control is symmetrical among

three phases under the balanced operation, we can develop its small-signal model just using the control in phase *a*, and drop the letter (*a*, *b*, and *c*) in the subscript. The time-domain relationship of the contribution of this control to the insertion index with equivalent module capacitor voltage and phase current in *d*-axis is denoted as

$$m_x = \cos\theta \cdot K_i \left[\left(K_{pvp} v_i + K_{pvi} \int v_i dt \right) \Big/ N + i_d \right]. \quad (14)$$

Because of the only existence of slight steady-state second harmonic in the right-side term of (14) under the balanced operation, the additional small-signal term at this control output caused by PLL dynamics is also very small, such that it can be ignored in the control model. Based on this assumption, the similar method used to linearize (11) can be applied to (14), then the small-signal form of (14) is expressed as

$$\hat{\mathbf{m}}_x = \mathbf{T}_c \mathbf{G}_{pv} \hat{\mathbf{v}}_i + K_i \mathbf{T}_c \hat{\mathbf{i}}_d \quad (15)$$

where $\mathbf{G}_{pv}$ is a 5 × 5 diagonal matrix defined as

$$\mathbf{G}_{pv} = \mathrm{diag}\left[\{ K_i \cdot H_{pv}(j2\pi(f_p + nf_1))/N \} |_{n=-2,-1,0,1,2} \right].$$

Based on Fig. 2, when the PLL is considered, the small-signal *d*-axis current can be denoted as

$$\hat{\mathbf{i}}_d = \mathbf{T}_d \hat{\mathbf{i}} + \mathbf{G}_p \hat{\mathbf{v}}_p \quad (16)$$

where $\mathbf{T}_d$ is a 5 × 5 tridiagonal matrix, of which elements in the main diagonal are zero, elements in the diagonal above main diagonal are {0, 1, 0, 0}, and elements in the diagonal below main diagonal are {1, 0, 0, 1}. $\mathbf{G}_p$ is a 5 × 5 matrix of which all elements are zero except for the (2, 3)th element, expressed as

$$G_\theta(j2\pi(f_p - f_1)) \cdot (I_1 e^{-j\alpha_1} - I_1 e^{j\alpha_1}).$$

By substituting (16) into (15), the phase voltage balancing control model is obtained as

$$\hat{\mathbf{m}}_x = \mathbf{T}_c \mathbf{G}_{pv} \hat{\mathbf{v}}_i + K_i \mathbf{T}_c \mathbf{T}_d \hat{\mathbf{i}} + K_i \mathbf{T}_c \mathbf{G}_p \hat{\mathbf{v}}_p. \quad (17)$$

In summary, an overall control model for the single-star MMC including phase current control and PLL as well as module capacitor voltage control by combining (5)–(7), (13), and (17) is

$$\hat{\mathbf{m}} = \mathbf{E} \hat{\mathbf{v}}_i + \mathbf{Q} \hat{\mathbf{i}} + \mathbf{P} \hat{\mathbf{v}}_p \quad (18)$$

where

$$\mathbf{E} = \mathbf{T}_c \mathbf{G}_v \mathbf{T}_0 + \mathbf{T}_c \mathbf{G}_{pv}, \ \mathbf{Q} = \mathbf{Q}_i + K_i \mathbf{T}_c \mathbf{T}_d,$$
$$\mathbf{P} = \mathbf{P}_p + K_i \mathbf{T}_c \mathbf{G}_p.$$

C. Impedance Response

Since the effects of capacitance in sub-modules, the arm currents in the power stage model (3) and (4) can be seen as the responses to both ac perturbation and module capacitor voltage perturbations. We consider the responses to the only ac voltage perturbation first by making the small-signal response of equivalent module capacitor voltage zero and substituting control model (18) into power stage model (3) and (4) to eliminate $\hat{\mathbf{m}}$, resulting in the following matrices:

$$\mathbf{Y}_{aa} = (\mathbf{U} + \mathbf{Y}_l \mathbf{V}_i \mathbf{Q})^{-1} \cdot (\mathbf{Y}_l - \mathbf{Y}_l \mathbf{V}_i \mathbf{P}) \quad (19)$$

$$\mathbf{Y}_{ma} = \mathbf{M}\mathbf{Y}_{aa} + \mathbf{I}(\mathbf{Q}\mathbf{Y}_{aa} + \mathbf{P}) \quad (20)$$

where $\mathbf{U}$ is a 5 × 5 unity matrix. $\mathbf{Y}_{aa}$ relates arm current $\hat{\mathbf{i}}$ to the grid voltage perturbation $\hat{\mathbf{v}}_p$ and $\mathbf{Y}_{ma}$ relates the module capacitor charging current $\hat{\mathbf{i}}_i$ to the grid voltage perturbation $\hat{\mathbf{v}}_p$. Therefore, we can define the (3, 3)th element in (19) in terms of the complex frequency *s* as

$$Y_{aa1}(s) = \hat{i}(s)/\hat{v}_p(s) \quad (21)$$

and the (2, 3)th and (4, 3)th element in (20), respectively, as

$$Y_{ma1}(s) = \hat{i}_i(s - j\omega_1)/\hat{v}_p(s) \quad (22)$$

$$Y_{ma2}(s) = \hat{i}_i(s + j\omega_1)/\hat{v}_p(s) \quad (23)$$

where $\omega_1 = 2\pi f_1$.

Similarly, when the responses to module capacitor voltage perturbation are considered independently, the control model (18) is introduced into the power stage model (3) and (4) and solved as

$$\mathbf{Y}_{am} = -(\mathbf{U} + \mathbf{Y}_l \mathbf{V}_i \mathbf{Q})^{-1} \cdot (\mathbf{Y}_l \mathbf{M} + \mathbf{Y}_l \mathbf{V}_i \mathbf{E}) \quad (24)$$

$$\mathbf{Y}_{mm} = \mathbf{M}\mathbf{Y}_{am} + \mathbf{I}(\mathbf{Q}\mathbf{Y}_{am} + \mathbf{E}) \quad (25)$$

where $\mathbf{Y}_{am}$ relates arm current $\hat{\mathbf{i}}$ to the module capacitor voltage perturbation $\hat{\mathbf{v}}_\mathbf{i}$ and $\mathbf{Y}_{mm}$ relates the module capacitor charging current $\hat{\mathbf{i}}_\mathbf{i}$to module capacitor voltage perturbation $\hat{\mathbf{v}}_\mathbf{i}$. The (3, 2)th and (3, 4)th element in (24) are defined in terms of the complex frequency *s*, respectively, as

$$Y_{am1}(s) = \hat{i}(s)/\hat{v}_i(s - j\omega_1) \quad (26)$$

$$Y_{am2}(s) = \hat{i}(s)/\hat{v}_i(s + j\omega_1) \quad (27)$$

and the (2, 2)th, (2, 4)th, (4, 2)th, and (4, 4)th element in (25) are defined, respectively, as

$$Y_{mm1}(s) = \hat{i}_i(s - j\omega_1)/\hat{v}_i(s - j\omega_1) \quad (28)$$

$$Y_{mm2}(s) = \hat{i}_i(s - j\omega_1)/\hat{v}_i(s + j\omega_1) \quad (29)$$

$$Y_{mm3}(s) = \hat{i}_i(s + j\omega_1)/\hat{v}_i(s - j\omega_1) \quad (30)$$

$$Y_{mm4}(s) = \hat{i}_i(s + j\omega_1)/\hat{v}_i(s + j\omega_1). \quad (31)$$

Since the transfer functions (22) and (23) are non-zero, the ac perturbation and module capacitor voltage perturbations are not independent. An ac voltage perturbation induces a current that charges the module capacitance to impose a module capacitor voltage perturbation, and then this module capacitor voltage perturbation induces an additional ac current that changes the converter responses. In addition, the transfer functions (28)–(31) indicate that the module capacitor voltage perturbations at different small-signal frequency are also related to each other. Such small signal flow from ac voltage perturbation to the arm current response at frequency f_p is represented in block diagram form in Fig. 4.

Based on this block diagram, the admittance model of single-star MMC as STATCOM with phase current control, PLL and

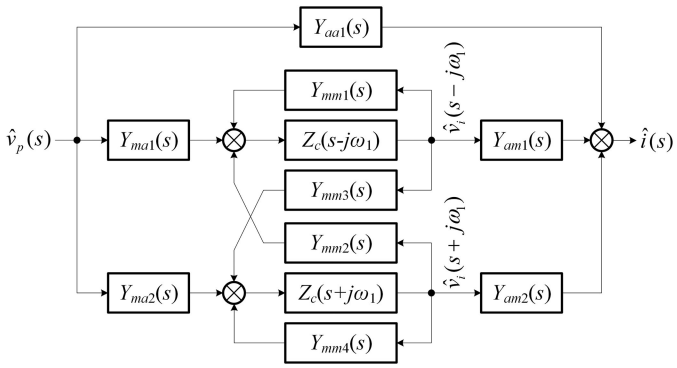

Fig. 4. Block diagram of small signal flow from ac voltage perturbation to arm current response at f_p.

TABLE I
PARAMETERS OF AN EXAMPLE 6 MVA STATCOM

Parameters	Values
Number of Modules per Arm	12
Arm Inductance	8 mH
Module Capacitance	2.7 mF
Cell Capacitor Voltage	1000 V
Grid L-L Voltage (RMS)	10 kV @ 50 Hz
Phase Current Controller	$H_i(s) = 5.9\times10^{-4} + 0.744/s$
PLL Controller	$H_\theta(s) = 0.016 + 3.077/s$
Average Voltage Controller	$H_v(s) = 0.269 + 23.578/s$
Phase Voltage Balancing Controller	$H_{pv}(s) = 0.088 + 1.38/s$ $K_i = 4.189\times10^{-4}$

TABLE II
SIMULATED RESULTS OF COMPLEX FOURIER COEFFICIENTS OF STATCOM

	Fourier Analysis of Time-Domain Response		
	Arm Current	Insertion Index	Equivalent Capacitor Voltage
dc	0.22×10^{-2}	1.31×10^{-6}	12000
f_1	489.75 ∠89.56°	0.74 ∠-0.04°	0.015 ∠138.82°
$2f_1$	0.99×10^{-2} ∠-46.76°	9.54×10^{-6} ∠-41.94°	1284.5 ∠-0.23°
$3f_1$	0.14 ∠137.09°	2.02×10^{-3} ∠2.04°	0.014 ∠134.58°

module capacitor voltage control can be obtained as (32) shown at the bottom of this page, where $Y_c(s) = {Z_c}^{-1}(s) = sC$.

Accordingly, the negative-sequence admittance can be obtained by replacing s in (32) by $-s$, and then taking the complex conjugate of each expression.

IV. MODEL VALIDATION

Small-signal sequence impedance can be measured by following the principle of harmonic linearization [3], which can be achieved by both computer simulation and experimental measurement. Since the computer simulation and experimental measurement have their merits, the developed models are validated by numerical simulation first and then by experimental measurement to support each other.

A. Simulation Validation

The computer simulation, which has been widely used for modeling and system analysis of power electronics in power systems, is a reliable tool for the validation of impedance of those high-power converters. An example high-power STATCOM with phase current control, PLL and module capacitor voltage control in Figs. 2 and 3 is built in MATLAB/Simulink to validate the developed impedance models. The parameters used in simulation are listed in Table I, where the control bandwidth is 200 Hz for the phase current control loop, 30 Hz for the PLL, 20 Hz for the average voltage control loop, 100 Hz for the current loop of phase voltage balancing control, and 2 Hz for the voltage loop of phase voltage balancing control, respectively. In addition, steady-state harmonics required for the power stage small-signal model are listed in Table II.

Impedance response of the converter is scanned numerically point by point from 1 Hz to 1 kHz. At each frequency, a voltage perturbation in either positive or negative sequence is injected and the converter is simulated for long enough time to enter steady-state. The response of the arm current at the perturbation frequency is extracted by Fourier analysis to calculate the input impedance. The scanned impedance responses are compared in Fig. 5 with the predicted impedance responses by the inverse of the admittance model (32). The two sets of responses are virtually identical over all frequencies, proving the accuracy of the model and correctness of the modeling method and approximations involved.

B. Experimental Validation

Based on the principle of harmonic linearization, a source of perturbation that has sufficient power and bandwidth, and can be connected in series with the grid voltage is required for the impedance validation; however, it is difficult to find such perturbation source and carry out the impedance measurement of an actual high-voltage high-power STATCOM in laboratory. One possible approach to provide experimental validation of the developed small-signal models would be to build a small-scale laboratory prototype of the MMC and measure its impedance [3], [23]. Obviously, such a scale-down prototype is different from actual converter in several aspects that do not scale with voltage and current, such as the number of modules, control delays, and amount of harmonics, but it can be used to evaluate the potential impacts on the responses, such as the discretized errors and parasitic component, to further validate the reasonability and accuracy of double-harmonic linearization based on the actual converter.

$$Y(s) = Y_{aa1}(s) + \frac{Y_{am1}(s)[(Y_c(s+j\omega_1) - Y_{mm4}(s))Y_{ma1}(s) + Y_{ma2}(s)Y_{mm2}(s)]}{(Y_c(s-j\omega_1) - Y_{mm1}(s))(Y_c(s+j\omega_1) - Y_{mm4}(s)) - Y_{mm2}(s)Y_{mm3}(s)} + \frac{Y_{am2}(s)[(Y_c(s-j\omega_1) - Y_{mm1}(s))Y_{ma2}(s) + Y_{ma1}(s)Y_{mm3}(s)]}{(Y_c(s-j\omega_1) - Y_{mm1}(s))(Y_c(s+j\omega_1) - Y_{mm4}(s)) - Y_{mm2}(s)Y_{mm3}(s)} \quad (32)$$

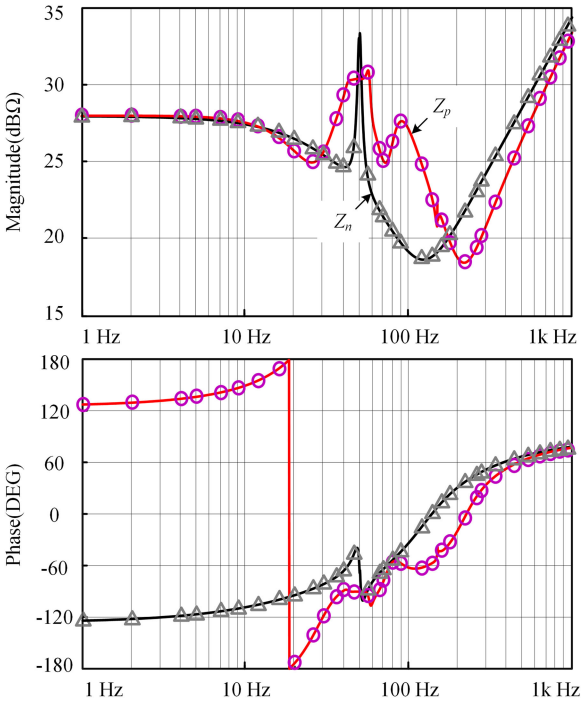

Fig. 5. Validation of the impedance responses of the example single-star STATCOM by comparing the developed models to the detailed circuit simulation: positive-sequence impedance (Z_p/circles) and negative-sequence impedance (Z_n/triangle).

TABLE III
PARAMETERS OF 10 KVA PROTOTYPE

Parameters	Values
Number of Modules per Arm	3
Arm Inductance	5.5 mH
Module Capacitance	1 mF
Cell Capacitor Voltage	140 V
Grid L-L Voltage (RMS)	380 V @ 50 Hz
Phase Current Controller	$H_i(s) = 0.023 + 58.49/s$
PLL Controller	$H_\theta(s) = 0.2 + 20/s$
Average Voltage Controller	$H_v(s) = 0.06 + 7/s$
Phase Voltage Balancing Controller	$H_{pv}(s) = 0.03 + 0.47/s$ $K_i = 0.016$

Therefore, a 10 kVA laboratory prototype of STATCOM in the single-star configuration is set up for the impedance measurement. The hardware architecture design of this prototype refers to a practical application of high-voltage high-power STATCOM, which consist of the master controller, slave controllers for each phase, executive controllers on their corresponding power sub-modules, high-speed LVDS board-to-board data transmission, and optical fiber communications. The control of this prototype is identical to that in Figs. 2 and 3, and its parameters are listed in Table III, where the control bandwidth is 400 Hz for the phase current control loop, 15 Hz for the PLL, and 20 Hz for the average voltage control loop, 200 Hz for the current loop of phase voltage balancing control, and 2 Hz for the voltage loop of phase voltage balancing control, respectively.

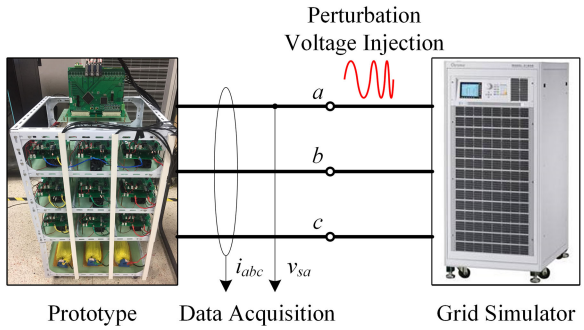

Fig. 6. Configuration of experimental measurement of a scale-down prototype impedance response.

The configuration of this experiment is illustrated in Fig. 6, where the Chroma Regenerative Grid Simulator Model 61860 is used as the three-phase grid, which the prototype is connected to, as well as the small-signal perturbation voltage injection source. The INTERHARMONIC function of this grid simulator allows performing frequency sweeps ranging from 1 to 1000 Hz superposed on the 50 Hz fundamental frequency. However, since this grid simulator cannot fully control the sequence of injected three-phase small-signal harmonics, we have to inject the perturbation voltage only in one phase (phase a), then acquire the data of three-phase currents and voltage of phase a though a high resolution oscilloscope, and calculate the magnitude and phase of these variables at the perturbation frequency f_p by Fourier analysis, which frequency spectrum resolution is set high (1 Hz) enough to guarantee the accuracy of small-signal frequency response measurement. Finally, the sequence impedance of this prototype can be obtained by

$$\mathbf{Z}(f_p) = \frac{\mathbf{v}_{sa}(f_p)}{\mathbf{i}_a(f_p) + \mathbf{i}_b(f_p)e^{\pm j2\pi/3} + \mathbf{i}_c(f_p)e^{\mp j2\pi/3}} \tag{33}$$

where the top of the $\pm$ and $\mp$ operators is to be used for positive-sequence impedance response and the bottom is to be used for negative-sequence impedance response. Noting that the impedance of the grid simulator may have effects on the impedance measurement results, but such effects are very limited in this experiment due to the much lower responses in the output terminal voltage at coupling frequencies, which indicates that the impedance of the grid simulator is low enough to be ignored [24].

The measured impedance responses are also compared with the predicted impedance responses by the inverse of the admittance model (32) using the parameters in Table III, presented in Fig. 7, where the steady-state harmonics required for the impedance models can be found by the solving of steady-state harmonic matrix equations or by numerical simulation. It is found that the impedance responses by experimental measurement match both the analytical positive-sequence and negative-sequence impedance responses very well. Compared to Fig. 5, the impedance responses of this scale-down prototype and the high-power STATCOM used in the simulation have similar characteristics due to the similar design of controls and their bandwidth. These confirm the validity of the developed impedance

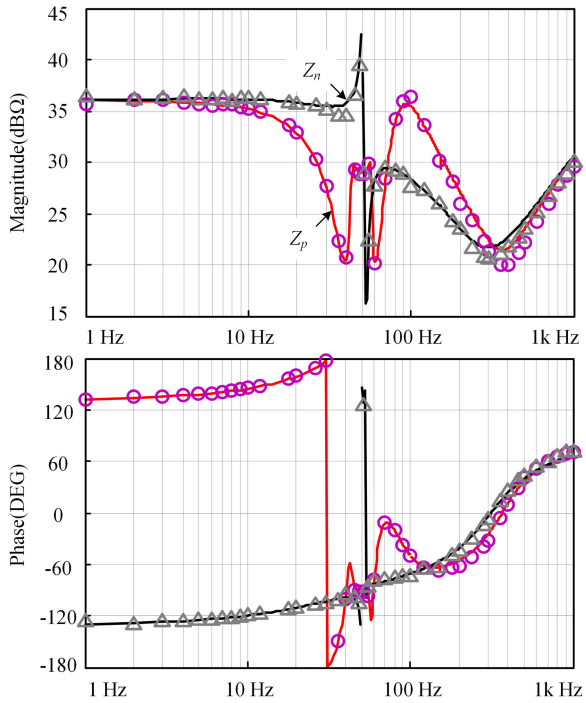

Fig. 7. Validation of the impedance responses of a scale-down prototype by comparing the developed models to the experimental measurement: positive-sequence impedance (Z_p/circles) and negative-sequence impedance (Z_n/triangle).

models based on double-harmonic linearization applied to the actual converters, as well as indicate that the discretized errors and parasitic component in this prototype do not cause a distinct difference on the impedance responses.

V. Impedance Characteristics Analysis

A. Comparison With Double-Star MMC

The symmetries among different arm currents, insertion indexes, and module capacitor voltages in a double-star MMC identified in [12] help to significantly reduce the power stage model to that of a single arm, such that the modeling of a double-star MMC and a single-star MMC seems similar, but actually is different due to their variant harmonics and controls. To fully understand the impedance characteristics of MMC, the developed small-signal model of single-star MMC is compared with double-star MMC that presented in [12].

The effects of harmonics on the impedance responses can be highlighted by the comparison of open-loop impedances of these two MMCs. By setting matrices **Q**, **P**, and **E** that represent the effects of control to zero in (19), (20), (24), and (25), we can obtain the algebraic expressions of transfer functions in (21)–(23) and (26)–(31) under the open-loop condition, where

$$Y_{aa1}(s) = 1/sL,\ Y_{ma1}(s) = M_1 e^{-j\gamma_1}/sL,$$
$$Y_{ma2}(s) = M_1 e^{j\gamma_1}/sL,\ Y_{am1}(s) = -M_1 e^{j\gamma_1}/sL,$$
$$Y_{am2}(s) = -M_1 e^{-j\gamma_1}/sL,$$
$$Y_{mm1}(s) = -{M_1}^2/sL - {M_1}^2/(s-2j\omega_1)L,$$

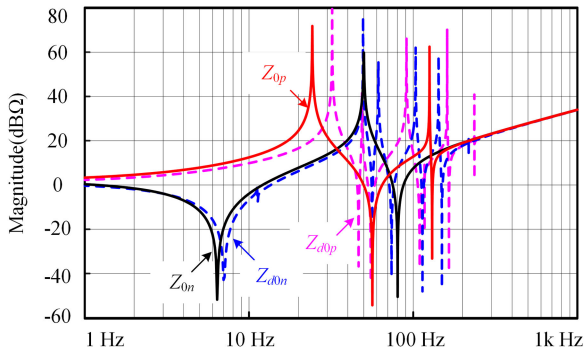

Fig. 8. Comparison of the open-loop impedance responses of single-star MMC (Z_0) and the open-loop single-arm impedance responses of double-star MMC (Z_{d0}).

$$Y_{mm2}(s) = -(M_1 e^{-j\gamma_1})^2/sL,$$
$$Y_{mm3}(s) = -(M_1 e^{j\gamma_1})^2/sL,$$
$$Y_{mm4}(s) = -{M_1}^2/sL.$$

Since these transfer functions can be seen as equivalent inductive admittances, based on (32), the open-loop impedance of single-star MMC is equivalent to a series and parallel connection of these inductive admittances and admittances of module capacitor at small-signal frequencies, which causes some resonances on the impedance responses.

Similarly, the open-loop impedance of double-star MMC presented in [12] also can be redefined using the block diagram form of small signal flow in Fig. 4. However, because of the complex harmonics caused by significant second-harmonic circulating current in double-star MMC, the number of module capacitor voltage perturbations increases to $2n+1$, whose frequencies vary from f_p–nf_1 to $f_p + nf_1$. Additionally, the double-star MMC as HVDC application is required to connect to a stiff dc bus, such that its insertion index usually includes an additional dc component compared to single-star MMC. Based on these features, more transfer functions, which consist of multiple equivalent inductive admittances at different small-signal frequencies in parallel, as well as admittances of module capacitor related to those module capacitor voltage perturbations should be considered in the open-loop impedance of double-star MMC, leading to more resonances on the impedance responses than signal-star MMC.

To confirm that, Fig. 8 shows the open-loop impedance response of the single-star MMC predicted by the model and compares it with the open-loop single-arm impedance response of a double-star MMC presented in [12]. The example single-star MMC as high-power STATCOM used in Section IV-A is applied, and the contrastive double-star MMC has similar circuit parameters and operation conditions with the single-star MMC to facilitate this comparison here and in the following. As can be seen, there are multiple resonances on the both positive- and negative-sequence open-loop impedance responses of the single-star MMC and the double-star MMC. Compared to the double-star MMC, the resonances on the impedance responses of single-star MMC are less and exist at different frequen-

cies. This demonstrates that the characteristics of open-loop impedance responses of MMC significantly depend on harmonics in the module capacitor voltage, arm current, and given insertion index, and the more complex harmonics MMC has, the more resonances its open-loop impedance responses have.

To understand the effects of current controls on the impedance response of MMC, these two MMCs with their each current control are compared. When the exclusive current control, namely phase current control, is considered in the single-star MMC, the corresponding transfer functions of (21)–(23) and (26)–(31) for impedance model can be obtained by setting matrix $\mathbf{Q}$ to $\mathbf{Q}_i$ and ignoring matrices $\mathbf{P}$ and $\mathbf{E}$ in (19), (20), (24), and (25). The algebraic expressions of transfer functions become too complex to be presented here completely, and one of them is taken as an example for the sake of clarity, which is this unnumbered equation shown at the bottom of this page, where $q_{11}(s)$ and $q_{33}(s)$ are the (1, 1)th and (3, 3)th elements in (5), respectively. It is found that compared to this transfer function under open-loop condition, impedances caused by the current controller are added in series and parallel with the impedances of arm inductor at small-signal frequencies to provide additional damping [25]. This effect of phase current control on transfer functions in (21)–(23) and (26)–(31) is similar, such that the resonances on the open-loop impedance responses of single-star MMC can be damped out when the phase current control is considered.

The current controls in the double-star MMC, including phase current control and circulating current control, have similar damping effects on the impedance responses. However, since the frequency separation between differential-mode (DM) and common-mode (CM) small-signal harmonics in double-star MMC [12], the additional impedances in the transfer functions caused by the phase current control and circulating current control mainly affect the impedances of arm inductor at the DM and CM small-signal frequencies, respectively. In other words, some resonances on impedance responses of double-star MMC caused by those inductive impedances of transfer functions at the CM small-signal frequencies cannot be alleviated without the circulating current control.

The comparison of the single-arm impedance responses of the double-star MMC with only phase current control and it with both phase current control and circulating current control is presented in Fig. 9. The parameters of circuit and phase current control and operation conditions are similar to the single-star MMC in Section IV-A, and a proportional resonant (PR) regulator tuned to the second-harmonic frequency is used in the circulating current control. Compared to the open-loop single-arm impedance responses of double-star MMC in Fig. 8, the phase current control has damped most resonances on both the positive- and negative-

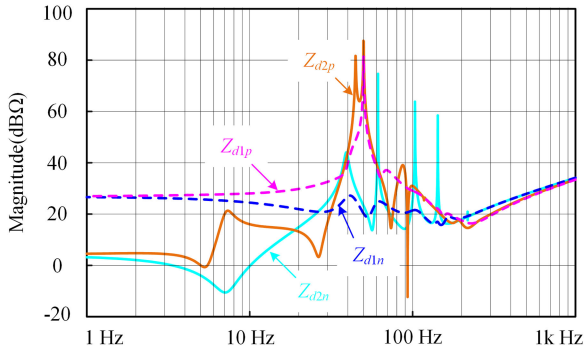

Fig. 9. Comparison of the single-arm impedance responses of double-star MMC with both phase current control and circulating current control (Z_{d1}) and it with only phase current control (Z_{d2}).

impedance responses, but still left a few resonances. When the circulating current control is activated, these left resonances are mitigated effectively. Additionally, the circulating current control improves the magnitude of impedance responses of double-star MMC below the fundamental frequency, which is helpful for the converter to enhance the stability.

The comparison of the impedances of the single-star MMC with phase current control and the single-arm impedances of the double-star MMC with phase current control and circulating current control is presented in Fig. 10. Since the impedance characteristics of the converter with an ideal PLL are usually dominated by the phase current control, the impedance responses of these two MMCs with the same bandwidth of phase current control are similar. The obvious difference on these two sets of impedances reflects in their responses at the low frequencies, of which the magnitude is decreased but the phase is increased due to the more equivalent admittance caused by complex harmonics in double-star MMC as well as the effects of circulating current control.

B. *Effects of Module Capacitor Voltage Control*

Since the single-star MMC as STATCOM application has no connection to a stiff dc bus, the module capacitor voltage control becomes indispensable under its normal operation. Based on (24) and (25), the effects of the first layer of module capacitor voltage control, namely average voltage control, can be equivalent to additional equivalent admittance added to the transfer functions $Y_{am1}(s)$, $Y_{mm1}(s)$, and $Y_{mm3}(s)$, which increases the magnitude of output admittance in (32) at low frequencies.

Since such effects mainly reflect in the positive-sequence impedance responses, Fig. 11 shows the comparison of the positive-sequence impedance responses of STATCOM with or

$$Y_{ma1}(s) = \frac{(M_1 e^{-j\gamma_1} + I_1 e^{-j\alpha_1} q_{33}(s))(V_{i0} q_{11}(s) + (s - 2j\omega_1)L)}{(V_{i0} q_{33}(s) + sL)(V_{i0} q_{11}(s) + (s - 2j\omega_1)L) - {V_{i2}}^2 q_{33}(s) q_{11}(s)} - \frac{(M_1 e^{j\gamma_1} + I_1 e^{j\alpha_1} q_{11}(s))(V_{i2} e^{-j\beta_2} q_{33}(s))}{(V_{i0} q_{33}(s) + sL)(V_{i0} q_{11}(s) + (s - 2j\omega_1)L) - {V_{i2}}^2 q_{33}(s) q_{11}(s)}$$

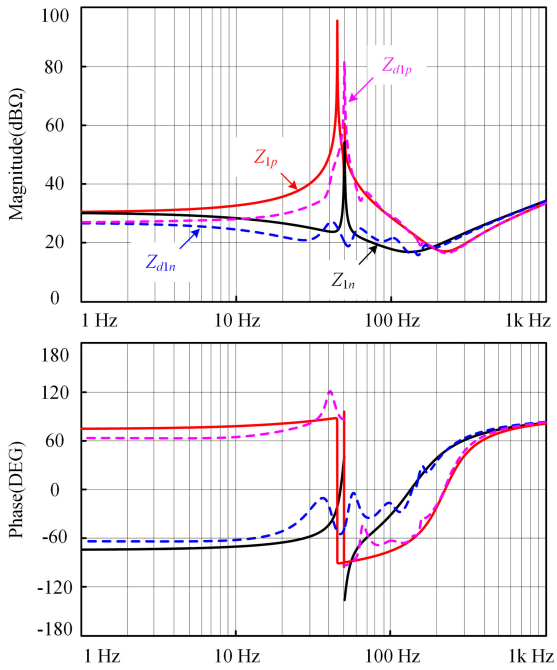

Fig. 10. Comparison of the impedance responses of single-star MMC with phase current control (Z_1) and the single-arm impedance responses of double-star MMC with phase current control and circulating current control (Z_{d1}).

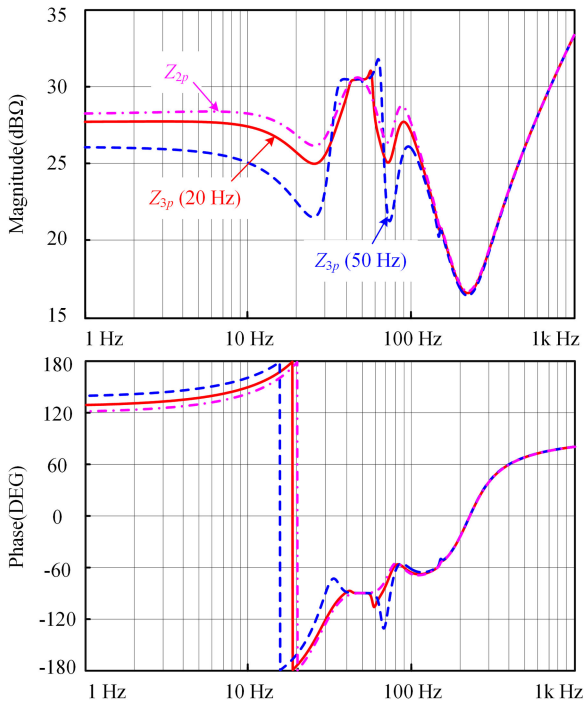

Fig. 11. Comparison of the positive-sequence impedance responses of STATCOM with different bandwidth of the average voltage control (Z_{3p}) and without this control (Z_{2p}).

without average voltage control, where the parameters of STATCOM is presented in Table I. The plotted impedance responses confirm the effects of average voltage control analyzed above. Additionally, Fig. 11 compares the effects of average voltage control with 20- and 50-Hz bandwidth design on the impedance responses. We can find that fast average voltage control

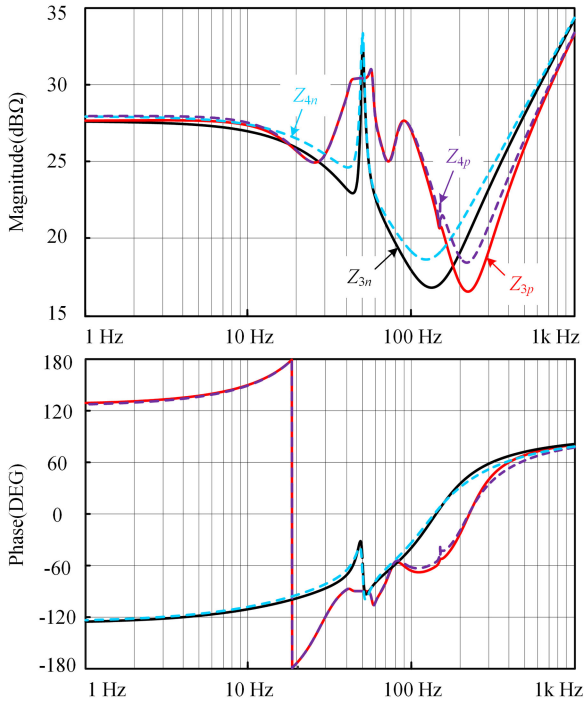

Fig. 12. Comparison of the impedance responses of STATCOM with the phase voltage balancing control (Z_4) and without this control (Z_3).

decreases the magnitude of impedance responses below 100 Hz sharply, except those impedance responses around the fundamental frequencies. Noting that this fast control specially leads to more dipping on both the magnitude and phase responses at the frequencies that dominated by the PLL, which is usually not desirable for gird-connected converters and should be avoided.

The second layer of module capacitor control, that is, phase voltage balancing control used in this paper consists of the voltage control loop and current control loop, which are similar to the average voltage control and phase current control, respectively, such that they have similar effects on the impedance responses. Based on (17), the phase voltage balancing control has effects on the gain of phase current control, PLL, and average voltage control; however, since the phase voltage balancing control is usually slow to avoid a conflict with that average voltage control and phase current control [19], such effects are too weak to cause significant difference on the impedance responses. The comparison of the impedance responses of STATCOM with or without this phase voltage balancing control is shown in Fig. 12, where the parameters of the phase voltage balancing control are also presented in Table I. As can be seen, except for the responses at the low frequencies as well as the bandwidth frequency of phase current control, there are almost no differences between these two sets of impedance responses. The difference at these frequencies is caused by the current control loop in the phase voltage balancing control that increases slightly the magnitude and phase of impedance responses, and such effects of phase voltage balancing control on the impedance responses help to enhance the stability of converter interacted with the grid.

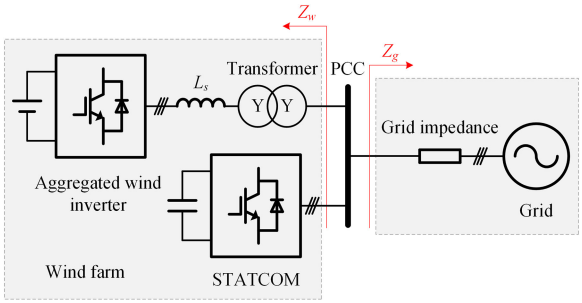

Fig. 13. Configuration of an example wind farm with STATCOM.

TABLE IV
PARAMETERS OF 30 MW AGGREGATED WIND INVERTER

Parameters	Values
Filter Inductance	9 μH
Filter Capacitance	13 mF
Leakage Inductance of Transformer	4 μH
DC Bus Voltage	1200 V
Grid L-L Voltage (RMS)	10 kV @ 50 Hz
Phase Current Controller	$H_i(s) = 2.67\times10^{-4} + 0.067/s$
PLL Controller	$H_\theta(s) = 0.27 + 80.75/s$

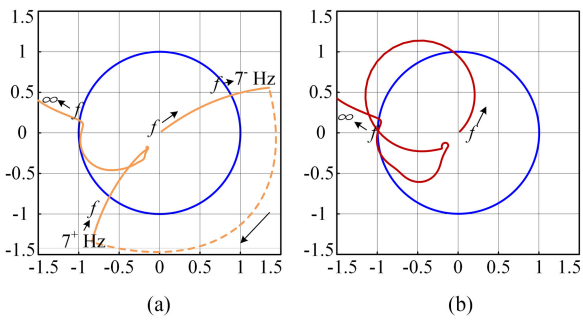

Fig. 14. Nyquist stability analysis. (a) Case 1, 20 Hz bandwidth of average voltage control in STATCOM. (b) Case 2, 50 Hz bandwidth of average voltage control in STATCOM.

VI. IMPEDANCE-BASED STABILITY ANALYSIS

An example wind farm with STATCOM connected to a weak grid in Western China is analyzed in this paper to account for the application of system stability analysis involving developed STATCOM impedance models. Fig. 13 shows the configuration of this representative wind power plant, where the wind farm is equipped with 20 1.5-MW direct-drive wind turbines based on two-level VSCs and LC filter and one 6 MVA STATCOM, introduced in Section IV-A. To simplify the system model, the 20 wind turbines are aggregated to a single 30 MW unit with the parameters listed in Table IV. A transformer is used to step up the inverter output voltage from 620 V to 10 kV and the leakage inductance of the transformer L_s serves as part of the inverter output filter. The grid is modeled as an ideal voltage source behind 7-mH grid impedance per phase, representing a weak grid with a short circuit ratio (SCR) of 1.5.

Based on Fig. 13, the stability of the currents injected to the point of common coupling (PCC) is determined by the impedance ratio Z_g/Z_w, which should satisfy the Nyquist stability criterion if the injected currents are stable [7]. Noting that the wind farm impedance Z_w can be expressed as a parallel connection of wind inverter impedance modeled in [26] and STATCOM impedance modeled in (32). Fig. 14 shows the Nyquist curves of Z_g/Z_w in positive sequence, where the wind turbine operates at unity power factor with 75% of rated power, and the STATCOM with phase current control, PLL and module capacitor voltage control operates under full load. Two cases are considered here: the bandwidth of average voltage control in the STATCOM is set to 20 Hz in Case 1 and 50 Hz in Case 2, and corresponding impedance characteristics of STATCOM for these two control bandwidth design have been analyzed in Section V-B. It can be seen that the Nyquist curve does not circle the point $(-1, 0j)$ in Case 1, which indicates that the currents injected to the grid are stable. However, the Nyquist curve approaches the point $(-1, 0j)$ gradually with the faster

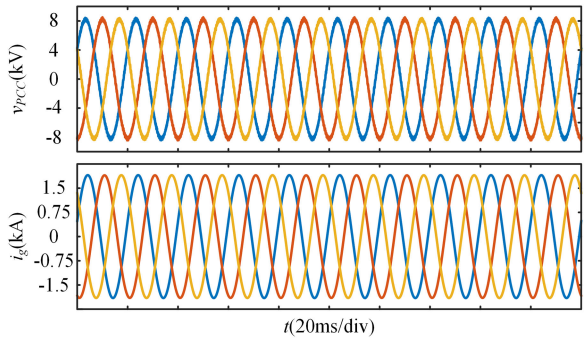

Fig. 15. Simulated results of three-phase PCC voltages and injected grid currents for Case 1.

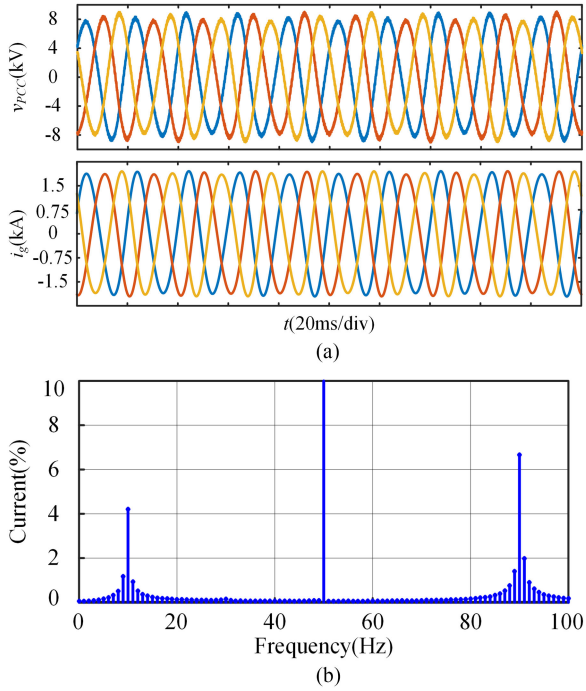

Fig. 16. Simulated results for Case 2. (a) Three-phase PCC voltages and injected grid currents. (b) FFT results of the current waveform.

average voltage control, and it encircles the $(-1, 0j)$ point once clockwise in Case 2, showing the instability.

Differing from the experimental validation of sequence impedance models of individual STATCOM, the computer simulation is considered to be an appropriate and acceptable method to verify system-level stability analysis due to the complexity of such practical application system. Fig. 15 shows the simulated results of this example wind farm with STATCOM for Case 1. The sinusoidal PCC voltages and injected grid currents without harmonics are consistent with the Nyquist plot in Fig. 14(a). And the simulated results of this example system for Case 2 are presented in Fig. 16. As can be seen, there are unstable resonances on the three-phase PCC voltage and injected grid current, and the FFT results of the injected grid currents show that resonance at 90 and 10 Hz, which likewise matches the Nyquist plot in Fig. 14(b).

VII. Conclusion

Impedance modeling of STATCOM based on MMC in single-star configuration is presented to characterize its frequency-domain behavior. Because of the absence of circulating current and its related control, the arm current in single-star configuration becomes harmonic-free. Based on this, a double-harmonic linearization method is proposed. In addition, the module capacitor voltage control for STATCOM is developed step-by-step to explain its effects on impedance responses. The developed models are validated by a high-power detailed switching circuit simulation and experimental measurement of a scale-down prototype, and also used to understand the effects of impedance behavior due to different control functions.

1) The complex harmonics in MMC cause some resonances on the open-loop impedance responses, but the current controls can provide some damping to mitigate these resonances and enhance the stability of the converter.
2) The fast average voltage control leads more dipping at the frequencies dominated by the PLL on positive-sequence impedance response, which should be avoided.
3) The phase voltage balancing control has no significant effects on the impedance responses, but increases slightly the robustness of impedances at the bandwidth frequency of phase current control.

Additionally, an example wind farm with STATCOM connected to a weak grid is presented to account for the application of system stability analysis using the developed STATCOM impedance models.

References

[1] I. Vieto and J. Sun, "Sequence impedance modeling and analysis of type-III wind turbines," *IEEE Trans. Energy Convers.*, vol. 33, no. 2, pp. 537–545, Jun. 2018.

[2] I. Vieto, G. Li, and J. Sun, "Behavior, modeling and damping of a new type of resonance involving type-III wind turbines," in *Proc. IEEE 19th Workshop Control Model. Power Electron.*, Jun. 2018, pp. 1–8.

[3] M. Cespedes and J. Sun, "Impedance modeling and analysis of grid-connected voltage-source converters," *IEEE Trans. Power Electron.*, vol. 29, no. 3, pp. 1254–1261, Mar. 2014.

[4] M. Cespedes and J. Sun, "Mitigation of inverter-grid harmonic resonance by narrow-band damping," *IEEE J. Emerg. Sel. Topics Power Electron.*, vol. 2, no. 4, pp. 1024–1031, Dec. 2014.

[5] H. Liu and J. Sun, "Analytical mapping of harmonics and impedance through phase-controlled converters," in *Proc. IEEE 13th Workshop Control Model. Power Electron.*, 2012, pp. 1–8.

[6] H. Liu and J. Sun, "Voltage stability and control of offshore wind farms with AC collection and HVDC transmission," *IEEE J. Emerg. Sel. Topics Power Electron.*, vol. 2, no. 4, pp. 1181–1189, Dec. 2014.

[7] J. Sun, "Impedance-based stability criterion for grid-connected inverters," *IEEE Trans. Power Electron.*, vol. 26, no. *11*, pp. 3075–3078, Nov. 2011.

[8] J. Sun *et al.*, "Renewable energy transmission by HVDC across the continent: System challenges and opportunities," *CSEE J. Power Energy Syst.*, vol. 3, no. 4, pp. 353–364, Dec. 2017.

[9] H. Saad, Y. Fillion, S. Deschanvres, Y. Vernay, and S. Dennetière, "On resonances and harmonics in HVDC-MMC station connected to AC grid," *IEEE Trans. Power Del.*, vol. 32, no. 3, pp. 1565–1573, Jun. 2017.

[10] J. Lyu, X. Cai, and M. Molinas, "Frequency domain stability analysis of MMC-based HVdc for wind farm integration," *IEEE J. Emerg. Sel. Topics Power Electron.*, vol. 4, no. 1, pp. 141–151, Mar. 2016.

[11] M. Beza, M. Bongiorno, and G. Stamatiou, "Analytical derivation of the ac-side input admittance of a modular multilevel converter with open- and closed-loop control strategies," *IEEE Trans. Power Del.*, vol. 33, no. 1, pp. 248–256, Feb. 2018.

[12] J. Sun and H. Liu, "Sequence impedance modeling of modular multilevel converters," *IEEE J. Emerg. Sel. Topics Power Electron.*, vol. 5, no. 4, pp. 1427–1443, Dec. 2017.

[13] M. A. Perez, S. Bernet, J. Rodriguez, S. Kouro, and R. Lizana, "Circuit topologies, modeling, control schemes, and applications of modular multilevel converter," *IEEE Trans. Power Electron.*, vol. 30, no. 1, pp. 4–17, Jan. 2015.

[14] S. Debnath, J. Qin, B. Bahrani, M. Saeedifard, and P. Barbosa, "Operation, control, and applications of the modular multilevel converter: A review," *IEEE Trans. Power Electron.*, vol. 30, no. 1, pp. 37–53, Jan. 2015.

[15] H. Akagi, "Classification, terminology, and application of the modular multilevel cascade converter (MMCC)," *IEEE Trans. Power Electron.*, vol. 26, no. 11, pp. 3119–3130, Nov. 2011.

[16] C. Li, R. Burgos, Y. Tang, and D. Boroyevich, "Impedance-based stability analysis of multiple STATCOMs in proximity," in *Proc. IEEE 17th Workshop Control Model. Power Electron.*, 2016, pp. 1–6.

[17] D. Shu, X. Xie, H. Rao, X. Gao, Q. Jiang, and Y. Huang, "Sub- and super-synchronous interactions between STATCOMs and weak AC/DC transmissions with series compensations," *IEEE Trans. Power Electron.*, vol. 33, no. 9, pp. 7424–7437, Sep. 2018.

[18] Y. Zhang, X. Chen, and J. Sun, "Impedance modeling and control of STATCOM for damping renewable energy system resonance," in *Proc. IEEEEnergy Convers. Congr. and Expo.*, 2017, pp. 3295–3302.

[19] H. Akagi, S. Inoue, and T. Yoshii, "Control and performance of a transformerless cascade PWM STATCOM with star configuration," *IEEE Trans. Ind. Appl.*, vol. 43, no. 4, pp. 1041–1049, Jul./Aug. 2007.

[20] D. Lu *et al.*, "Clustered voltage balancing mechanism and its control strategy for star-connected cascaded H-bridge STATCOM," *IEEE Trans. Ind. Electron.*, vol. 64, no. 10, pp. 7623–7633, Oct. 2017.

[21] Q. Song and W. Liu, "Control of a cascade STATCOM with star configuration under unbalanced conditions," *IEEE Trans. Power Electron.*, vol. 24, no. 1, pp. 45–58, Jan. 2009.

[22] H. C. Chen *et al.*, "Zero-sequence voltage injection for dc capacitor voltage balancing control of the star-connected cascaded H-bridge PWM converter under unbalanced grid," *IEEE Trans. Ind. Appl.*, vol. 51, no. 6, pp. 4584–4594, Nov./Dec. 2015.

[23] J. Lyu, X. Zhang, X. Cai, and M. Molinas, "Harmonic state-space based small-signal impedance modeling of a modular multilevel converter with consideration of internal harmonic dynamics," *IEEE Trans. Power Electron.*, vol. 34, no. 3, pp. 2134–2148, Mar. 2019.

[24] I. Vieto and J. Sun, "Sequence impedance modeling and converter-grid resonance analysis considering dc bus dynamics and mirrored harmonics," in *Proc. IEEE 19th Workshop Control Model. Power Electron.*, 2018, pp. 1–8.

[25] M. Cespedes and J. Sun, "Impedance shaping of three-phase grid-parallel voltage-source converters," in *Proc. IEEE 27th Annu. IEEE Appl. Power Electron. Conf. Expo.*, 2012, pp. 754–760.

Yang Zhang (S'17) was born in Fujian Province, China, in 1989. He received the B.S. and M.S. degrees in electrical engineering, in 2012 and 2015, respectively, from the Nanjing University of Aeronautics and Astronautics, Nanjing, China, where he is currently working toward the Ph.D. degree in electrical engineering.

His main research interests include the renewable generation system modeling, stability analysis, and control.

Xin Chen (S'99–M'04) received the B.S. and Ph.D. degrees in electrical engineering from Nanjing University of Aeronautics and Astronautics, Nanjing, China, in 1996 and 2001, respectively.

He is a Professor and the Chair with the Department of Electrical Engineering, Nanjing University of Aeronautics and Astronautics. From 2001 to 2003, he was a Chief Engineer with Power Division, ZTE Corporation, and from 2010 to 2011, he was a Visiting Scholar with Rensselaer Polytechnic Institute, Troy, MI, USA. His current research interests include modeling, control and stability of distributed generation, and microgrid systems.

Jian Sun (M'95–SM'09–F'15) received the B.S. degree from the Nanjing Institute of Aeronautics, Nanjing, China, in 1984, the M.S. degree from the Beijing University of Aeronautics and Astronautics, Beijing, China, in 1989 and the Dr. Eng. degree from the University of Paderborn, Paderborn, Germany, in 1995, all in electrical engineering.

He was a Post-doctoral Fellow with the School of Electrical and Computer Engineering, Georgia Institute of Technology, from 1996 to 1997. He worked with Advanced Technology Center, Rockwell Collins, Inc., from 1997 to 2002, where he led research on advanced power conversion for aerospace applications. In August 2002, he joined Rensselaer Polytechnic Institute in Troy, NY, USA, where he is currently a Professor and Director of the New York State Center for Future Energy Systems. He has published more than 200 journal and conference papers on these subjects, and holds 12 U.S. patents. His research interests include the general area of power electronics and energy conversion, with a focus on modeling, control, as well as applications in aerospace and renewable energy systems.

Dr. Sun served as the Editor-in-Chief of the IEEE POWER ELECTRONICS LETTERS from 2008 through January 2014. He also served as Chair of the IEEE Power Electronics Society's Technical Committee on Power and Control Core Technologies until December 2012 and became the Treasurer of PELS in January 2013. He was the General Chair of IEEE COMPEL'06 Workshop and was involved in the organization of numerous other IEEE conferences. He was the recipient of the IEEE Power Electronics Society Modeling and Control Technical Achievements Award in 2013 and the David R. Middlebrook Outstanding Achievement Award in 2017.